# Naval Research Laboratory

Washington, DC 20375-5320

# Calculation of the Ionospheric O+ Concentration From O II 834 Å Airglow Using Discrete Inverse Theory

J.M. PICONE
R.R. MEIER
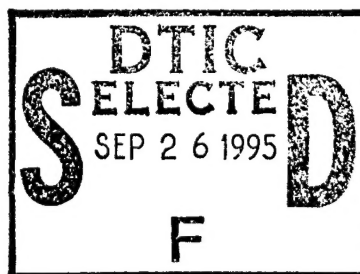K.F. DYMOND
R.P. McCOY

*E.O. Hulburt Center for Space Research*

O. KELLEY

*George Mason University*
*Fairfax, VA 22030*

R.J. THOMAS

*New Mexico Institute of Mining and Technology*
*Socorro, NM 87801*

DTIC
SELECTED
SEP 2 6 1995
F

19950922 124

September 1, 1995

DTIC QUALITY INSPECTED 1

# REPORT DOCUMENTATION PAGE

| 1. AGENCY USE ONLY *(Leave Blank)* | 2. REPORT DATE September 1, 1995 | 3. REPORT TYPE AND DATES COVERED Memo Report 1 Oct 1991-1 July 1995 |
|---|---|---|

**4. TITLE AND SUBTITLE**

Calculation of the Ionospheric $O^+$ Concentration From O II 834 Å Airglow Using Discrete Inverse Theory

**5. FUNDING NUMBERS**

PE-61153N
PE-63716D
PE-35160F

**6. AUTHOR(S)**

J.M. Picone, R.R. Meier, O. Kelley,* K.F. Dymond, R.J. Thomas,** and R.P. McCoy

**7. PERFORMING ORGANIZATION NAME(S) AND ADDRESS(ES)**

Naval Research Laboratory
Washington, DC 20375-5320

**8. PERFORMING ORGANIZATION REPORT NUMBER**

NRL/MR/7643--95-7772

**9. SPONSORING/MONITORING AGENCY NAME(S) AND ADDRESS(ES)**

Office of Naval Research
800 North Quincy Street
Arlington, VA 22217-5660

**10. SPONSORING/MONITORING AGENCY REPORT NUMBER**

**11. SUPPLEMENTARY NOTES**

*Institute for Computational Sciences and Informatics, George Mason Univ., Fairfax, VA 22030
**Department of Electrical Engineering, New Mexico Institute of Mining and Tech., Socorro, NM 87801

**12a. DISTRIBUTION/AVAILABILITY STATEMENT**

Approved for public release; distribution unlimited.

**12b. DISTRIBUTION CODE**

**13. ABSTRACT** *(Maximum 200 words)*

Discrete inverse theory (DIT) forms the basis of new techniques for extracting dayside $O^+$ number density profiles from the 834 Å airglow, as measured by a limb-scanning system on an orbiting satellite. Our tests of this method assume observations from an altitude of 850 km with scans from 10° to 26.5° below horizontal, consistent with future multiyear missions. The retrieval code computes an iterative, maximum likelihood solution by comparing observations to estimates calculated with a new forward model. The model includes multiple resonant scattering and pure absorption. To generate synthetic data for tests, we represent the "true" $O^+$ distribution as a Chapman layer and compute an intensity profile with the forward model, adding simulated noise. We present detailed studies of convergence properties of the retrieval techniques and of uncertainties in the retrieved parameters. For this baseline (Chapman layer) case, the method is robust, converging to an accurate solution for a wide variation in synthetic data. We include a brief preview of recent studies showing the following: (1) for future missions, the DIT method can correctly distinguish between distinctly different Chapman layers that produce nearly identical intensity profiles and (2) the retrieval of an additional parameter that scales the model intensity profile can compensate for inaccuracies in the instrument sensitivity or in the magnitude of the initial volume excitation rate.

**14. SUBJECT TERMS**

Remote sensing
Computer algorithms
Ionosphere
Discrete inverse theory
Upper atmosphere

**15. NUMBER OF PAGES**

31

**16. PRICE CODE**

| 17. SECURITY CLASSIFICATION OF REPORT | 18. SECURITY CLASSIFICATION OF THIS PAGE | 19. SECURITY CLASSIFICATION OF ABSTRACT | 20. LIMITATION OF ABSTRACT |
|---|---|---|---|
| UNCLASSIFIED | UNCLASSIFIED | UNCLASSIFIED | UL |

# CONTENTS

# CALCULATION OF THE IONOSPHERIC O+ CONCENTRATION FROM O II 834 Å AIRGLOW USING DISCRETE INVERSE THEORY

## 1. Introduction

The $O^+$ ($2s^2$ $2p^3$ $^4S^o \leftarrow$ $2s$ $2p^4$ $^4P$) transition produces a triplet emission at line center wavelengths of 832.76, 833.33, and 834.47 Å [Eriksson, 1987]. This is the brightest O II feature observed in the ultraviolet (UV) dayglow [Meier, 1991]. The 834 Å triplet transition is an allowed multiplet, for which the photons undergo multiple resonant scattering by $O^+$ ions in the F layer of the ionosphere. This process significantly enhances the 834 Å volume emission rate in the vicinity of the F-layer, so that different $O^+$ distributions can produce qualitatively different F-layer limb intensity profiles [McCoy et al., 1985]. The purpose of the present work is to demonstrate new techniques for the retrieval of altitude profiles of the $O^+$ number density from observations of the O II 834 Å airglow by a limb-scanning extreme ultraviolet (EUV) spectrograph. Because $O^+$ is the dominant ion in the F region of the ionosphere, these methods can transform 834 Å limb intensity data into electron density maps of the F region.

This work supports a number of multiyear satellite-borne systems for remote sensing of the upper atmosphere; the observations will take place over the next fifteen years and should continue well beyond that period. These systems include the Remote Atmospheric and Ionospheric Detection System (RAIDS), for which a new host platform has not yet been identified [McCoy et al., 1994a; Christensen et al., 1993]; the Advanced Research and Global Observation Satellite (ARGOS; McCoy [1995]), due for launch in 1996; and the Special Sensor Ultraviolet Limb Imager (SSULI: McCoy et al. [1994b]), which will be flown by the Defense Meteorological Satellite Program (DMSP) on a series of five missions possibly beginning as early as 1997. All of these systems will occupy polar, Sun-synchronous, circular orbits at altitudes between 800 and 900 km and will scan the limb of the Earth within an angular range of approximately 10° to 26.5° below the horizontal. All missions carry instruments that provide spectral resolution of 12 to 15 Å in the EUV band and 7 to 11 Å in the FUV band. Given the similarity of the respective measurements, these missions will provide a long-term, self-consistent data set for detailed global studies of the dynamical behavior of the upper atmosphere as a function of various geophysical parameters and forcing agents, e.g., solar and geomagnetic activity. In addition, the database should be useful in developing more accurate empirical and *ab initio* models of the upper atmosphere.

McCoy et al. [1985] laid the foundation for these developments by performing detailed parametric studies of the relationships between various geophysical and ionospheric parameters and O II 834 Å airglow measurements from a spinning satellite (STP78-1). The work relied primarily on a radiative transport model that included the effects of multiple resonant scattering by $O^+$ and pure absorption (extinction) of photons by O, $N_2$, and $O_2$ [Anderson and Meier, 1985]. To determine the location and rate of photon production, including both photoionization and photoelectron impact ionization of atomic oxygen, McCoy et al. used the PEGFAC code of Strickland and Meier [1982]. A standard Chapman layer represented the $O^+$ distribution in the altitude variable z :

$$N_{O^+}(z) = N_{max} \exp\left[\frac{1}{2}\left(1 - \frac{z - z_{max}}{H} - \exp\left\{-\frac{z - z_{max}}{H}\right\}\right)\right] \qquad (1)$$

where $N_{O^+}$ is the $O^+$ number density at a given altitude, $z_{max}$ is the altitude at which the $O^+$ number density peaks, $N_{max}$ is the peak $O^+$ number density, and H is the (neutral) atomic oxygen scale height. The study indicated that the solar flux, the photoelectron flux, and the neutral number density distributions mainly affected the magnitude of the intensity profiles while the shape changed little. On the other hand, changes in the Chapman parameters [$N_{max}$, $z_{max}$, H] caused distinct changes in the shape of the intensity profile, suggesting that these parameters could be retrieved from the data.

The present paper presents a thorough analysis of efficient methods for retrieving an optimal $O^+$ number density distribution from 834 Å limb intensity measurements. The basis for the methods is discrete inverse theory (DIT: Rodgers [1976], Tarantola [1987], Tarantola and Valette [1982], Menke [1989]), which has been introduced by Meier and Picone [1994] for the retrieval of thermospheric composition and temperature from far ultraviolet (FUV) limb intensity profiles. To establish a direct connection to the work of McCoy et al. [1985] and to provide an assessment of the potential of DIT for moderately optically thick systems, we have used the Chapman layer representation of the $O^+$ distribution in the F region, as given by Equation (1). This representation has been useful for both qualitative and quantitative analysis of the F region [Kelley and Heelis, 1989; Chamberlain and Hunten, 1987]. On the other hand, Anderson et al. [1987] have pointed out that Equation (1) is not general enough to provide close fits to profiles produced by sophisticated simulation models. D. N. Anderson and M. Fox [private communication, 1993] have suggested generalizations of the Chapman layer with additional parameters. The present paper will provide a useful baseline for assessing more robust representations of the $O^+$ distribution.

The specific task covered by this paper, therefore, is to retrieve the three Chapman parameters underlying synthetic limb intensity data that are consistent with the sensitivity and observational geometry of the systems mentioned above. We follow the presentation of Meier and Picone [1994] on the retrieval of thermospheric composition and temperature from the FUV dayglow. The key difference is that Meier and Picone neglected resonant scattering effects, while such effects are significant in the case of the O II 834 Å field. Multiple scattering can enhance the volume emission rate in the F-layer; on the other hand, a sizable loss of information can occur along the line of sight. These effects increase the complexity and nonlinearity of the forward model.

Section 2 presents a summary of discrete inverse theory and discusses the forward model for calculating the limb intensity during the retrieval. We use the same model to generate synthetic data as well. The Appendix outlines the numerical algorithm used for computing volume excitation rates according to the prescription in Section 2. Section 3 describes the model system and the simulated observations used for testing the DIT code. The tests employ the representation of the $O^+$ number density given by Equation (1) both to generate synthetic data

and, as part of the DIT forward model, to estimate intensity values during the retrieval process. As a result, the tests assume that the DIT forward model constitutes an accurate representation of the true physical system. Consequently, the results provide an upper bound on the performance of DIT for this application.

Section 4 discusses the convergence properties of the algorithms and the sensitivity to the initial conditions for the iterative process. We then provide a picture of the uncertainties in the retrieved Chapman parameters as functions of the "true" parameter values used to generate the synthetic data. Section 5 uses the "concentration scalar model" (CSM) of Meier and Picone [1994] and R. Thomas [private communication, 1993] to assess the sensitivity of limb-scanning experiments to the $O^+$ density at different altitudes within the F-layer. Section 6 summarizes the main results of the study and discusses the details involved in producing comprehensive, practical O II 834 Å inversion algorithms which are customized to various scientific and engineering applications. Because of the interest generated by recent conference presentations [Picone et al., 1994; Kelley et al., 1994] and publications [Link et al., 1994], Section 6 includes a brief preview of ongoing studies [Picone et al., 1995a,b] addressing the following issues:
(1) the retrieval of an additional parameter to scale the intensity data and
(2) the problem of faithfully retrieving distinctly different $O^+$ number density profiles which correspond to "nearly identical" intensity profiles.

## 2. Inversion Technique

### 2.1. Discrete Inverse Theory (DIT)

Meier and Picone [1994] have reviewed the primary features of Menke's [1989] presentation of DIT with nonlinear forward models. This formulation, which is based on a maximum likelihood criterion, applies specifically to cases in which the distributions of data points and model parameters about their respective mean values are approximately Gaussian. Here we briefly describe and extend the discussion of Meier and Picone to include the relationship of Menke's approach to others.

Consider a set of discrete observational data which may be expressed as components of a vector $\mathbf{d}^o$ of length $N$. In the present context, this vector contains limb intensity measurements as a function of observation zenith angle (OZA). In order to extract information regarding the concentration of the emitting species, we require a forward model,

$$\mathbf{G}(\mathbf{m}) = \mathbf{d}, \tag{2}$$

in which $\mathbf{m}$ is a vector of parameters defining the spatial distribution of the emitting species and the vector $\mathbf{d}$ is the "model" limb intensity, computed as a function of OZA for a given $\mathbf{m}$. The vector function $\mathbf{G}$ thus maps a species density distribution onto a limb intensity profile corresponding to a particular scan. We denote the number of parameters, and hence the length of $\mathbf{m}$, by the variable $M$. For the present tests of our algorithms, the number of parameters, $M$, is three and $\mathbf{m} = [N_{max}, z_{max}, H]$, the vector containing the Chapman parameters in Equation (1).

As we will show in the next subsection, the model limb intensity vector $\mathbf{G}(\mathbf{m})$ is a highly nonlinear function of the $O^+$ number density and the major neutral constituents. To compute parameter values, we, therefore, use an iterative technique equivalent to that of Meier and Picone [1994]. We seek the maximum likelihood solution for cases in which both the data and model parameters are distributed normally, i. e.,

$$P(\mathbf{d}, \mathbf{d}^o) \propto \exp\left\{ -\frac{1}{2} (\mathbf{d} - \mathbf{d}^o)^T [\mathbf{cov}\ \mathbf{d}]^{-1} (\mathbf{d} - \mathbf{d}^o) \right\} \tag{3}$$

and

$$P(\mathbf{m}, \langle \mathbf{m} \rangle) \propto \exp\left\{ -\frac{1}{2} (\mathbf{m} - \langle \mathbf{m} \rangle)^T [\mathbf{cov}\ \mathbf{m}]^{-1} (\mathbf{m} - \langle \mathbf{m} \rangle) \right\}. \tag{4}$$

In Equation (3), [$\mathbf{cov}\ \mathbf{d}$] is the covariance matrix for the data. In Equation (4), $\langle \mathbf{m} \rangle$ is the vector of *a priori* model parameter values, which provide estimates of the parameter values to be retrieved, and [$\mathbf{cov}\ \mathbf{m}$] is the covariance matrix of the *a priori* model parameter values. The *a priori* model parameter vector permits the calculation of the optimum estimate of model parameters when the problem is underdetermined or mixed-determined. Possible sources for values of $\langle \mathbf{m} \rangle$ include results from the analysis of prior data sets (e.g., preceding limb scans), semi-empirical models, or theoretical constraints or estimates.

4

To obtain the maximum likelihood solution for a given set of observations and for the corresponding *a priori* model parameter values, we compute the best estimate $\mathbf{m}^e$ of the vector $\mathbf{m}$ which maximizes the joint probability

$$P(\mathbf{m}, \mathbf{d}) \propto P(\mathbf{m}, \langle \mathbf{m} \rangle)\, P(\mathbf{d}, \mathbf{d}^o) \ , \tag{5}$$

subject to the constraint of Equation (2). Hence we must minimize the generalized $\chi^2$, given by

$$\chi^2 = (\mathbf{d} - \mathbf{d}^o)^T\, [\mathbf{cov}\ \mathbf{d}]^{-1}\, (\mathbf{d} - \mathbf{d}^o) + (\mathbf{m} - \langle \mathbf{m} \rangle)^T\, [\mathbf{cov}\ \mathbf{m}]^{-1}\, (\mathbf{m} - \langle \mathbf{m} \rangle) \ . \tag{6}$$

One well-known method of accomplishing this is the Levenberg-Marquardt method (LM: e.g., see Press et al. [1989]). Meier and Picone [1994] presented an alternative method based on the formulation of Menke [1989] (also Tarantola [1987]). The two methods provide a solution when the forward model, Equation (2), is nonlinear. Both start with an initial estimate, $\mathbf{m}^e_0$, and iteratively solve an approximate equation in which the solution at step $(n + 1)$ depends both on $\mathbf{m}^e_n$, the estimate of the model parameters after the $n^{th}$ iteration, and on the gradient, $\nabla \mathbf{G}_n$, of the forward model with respect to $\mathbf{m}$, evaluated at $\mathbf{m} = \mathbf{m}^e_n$. Thus, no higher derivatives of the forward model occur in the procedures. Unlike the calculations of McCoy et al. [1985], the methods allow all parameters to change at each computational step. In our implementation, the only numerical approximation of note is the use of one-sided derivatives to estimate the gradient matrix $\nabla \mathbf{G}_n$. Higher-order derivatives require that the forward model be evaluated at more points in parameter space. The concomitant increased expense has proven to be more significant than any loss of accuracy in the search for an optimum solution. For the tests in this paper, the procedure has "converged" when the change in successive values of $\chi^2$ is $10^{-4}$ or less. Comparison with results based on more stringent convergence criteria have shown that the use of $10^{-4}$ translates into an uncertainty in the range of $\pm 2\%$ for $\mathbf{m}^e$.

From the presentation of LM by Press et al. and the discussion of the alternative method by Tarantola [1987], we have found, in fact, that the two formulations (i.e., Menke and LM) are equivalent when applied to the generalized $\chi^2$ of Equation (6). (Note that Press et al. deal specifically with the overdetermined case and do not allow for *a priori* data with a finite covariance.) Tarantola calls this a "quasi-Newton method," which has superior convergence properties in comparison to the method of steepest descent. The only formal difference between the two approaches lies in selecting the size of the change in the model parameter vector from iteration to iteration. As the optimum value of $\mathbf{m}^e$ is approached, one would prefer to take smaller steps, because of the numerical and analytic approximations that are involved. If the step size is too large on the $n^{th}$ iteration, for example, the $n^{th}$ estimate, $\mathbf{m}^e_n$, might actually be farther from the region of convergence than is $\mathbf{m}^e_{n-1}$. Thus satisfactory convergence might never be achieved. LM checks for this specific situation, adjusting the step size iteratively to ensure better convergence at each step. Menke includes no corresponding calculation of optimal step size. Fortunately the user can incorporate the LM step size selection procedure into Menke's equations. Tarantola also provides analytic methods of choosing an appropriate step size; we have not investigated his analytic estimates.

5

## 2.2. Estimating Uncertainties in Retrieved Model Parameters

Of nearly equal importance with the retrieval of model parameters is the ability to estimate the uncertainties in both the retrieved parameter values and the values of the physical quantities which have been parameterized. In our case, the parameterized physical quantity is the $O^+$ number density as a function of altitude. Here Menke [1989] and Tarantola and Valette [1982] transcend the LM approach by providing an estimate of the covariance matrix for $m^e$, based on the results for the general, linear Gaussian case:

$$\left[\text{cov } m_n^e\right] \cong \nabla G_n^{inv} \left[\text{cov d}\right] (\nabla G_n^{inv})^T + \left[\hat{I} - R_n\right]\left[\text{cov m}\right]\left[\hat{I} - R_n\right]^T$$
$$= \left(\nabla G_n^T \left[\text{cov d}\right]^{-1} \nabla G_n + \left[\text{cov m}\right]^{-1}\right)^{-1} . \tag{7}$$

In Equation (7), $m_n^e$ is the estimate for the optimum model parameter vector after the $n^{th}$ iteration, $\nabla G_n^{inv}$ is the "generalized inverse matrix" for the gradient $\nabla G_n$ of the forward model, $\hat{I}$ is the identity matrix for model parameter space, and the "model resolution matrix" is [Tarantola, 1987; Menke, 1989]:

$$R_n \equiv \nabla G_n^{inv} \nabla G_n . \tag{8}$$

For an overdetermined case (e.g., Chapman layer representation with $N > 3$), $R_n = \hat{I}$. On the other hand, the retrieval problem is often mixed-determined [Menke, 1989] when the concentration scalar model is used (Section 5), and $R_n \neq \hat{I}$. The standard deviation $\sigma_i = ([\text{cov } m^e]_{ii})^{1/2}$ gives a measure of the uncertainty in the retrieved model parameter $m_i^e$.

If the forward model equations or their numerical solutions are approximate, or if the forward model depends on quantities that are not known precisely (e.g., the values of cross sections), Menke [1989] and Tarantola [1987] represent the model estimates of $d$ by a Gaussian distribution about $G(m)$ with a covariance matrix, $[\text{cov G}]$, that corresponds to the uncertainty in the estimates. Equation (5) then must include this distribution as a third multiplicative factor, rather than assuming the exact constraint of Equation (2). Equation (6), Equation (7), and the definition of $\nabla G_n^{inv}$ then hold with $[\text{cov d}]$ replaced by $[\text{cov d}] + [\text{cov G}]$ [Tarantola and Valette, 1982] . These modifications permit an assessment of the effects of approximations in the forward model and of uncertainties in inputs to the forward model on the overall uncertainty in the retrieved model parameters. The intent of the present paper is to provide a baseline for such assessments; thus we assume that the constraint of Equation (2) is exact.

To convert the uncertainties in the model parameters, as represented by $[\text{cov } m^e]$, to the uncertainty in the $O^+$ number density at a given altitude, we use the standard formula for propagation of errors [Bevington and Robinson, 1992]:

6

$$\text{var}\left[N_{O^+}(z)\right] \cong \sum_i \sum_j \left[\text{cov } \mathbf{m}^e\right]_{ij} \left(\frac{\partial N_{O^+}(z)}{\partial m_i}\right) \left(\frac{\partial N_{O^+}(z)}{\partial m_j}\right) . \quad (9)$$

Here the term "var" represents the variance, i.e., the square of the standard deviation. We evaluate the derivatives using Equation (1) with the retrieved model parameter values.

Since the covariance matrix is symmetric, [cov $\mathbf{m}^e$] has $\frac{1}{2}(M^2 + M)$ independent elements. Equation (9), therefore, can provide realistic estimates of the uncertainties at each of a large number of grid points only if Equation (1) accurately represents the true $O^+$ number density distribution. In that case, Equation (1) can provide a faithful extrapolation of the $O^+$ number density to altitudes which are not well-sampled by the observing instrument.

To determine the amount of information that the instrument is receiving from each region of the upper atmosphere, we may generate synthetic data using a Chapman layer or another model and then use the concentration scalar model (CSM) to represent the $O^+$ number density profile in the retrieval code [Meier and Picone, 1994]. The CSM specifies a set of $M$ ($\leq N$) altitude grid points at each of which the $O^+$ number density is itself treated as a model parameter independent of the number density at any other altitude point. In contrast to Equation (1) or semi-empirical models, the densities at different grid points are not coupled. The CSM number density profile, therefore, cannot extrapolate values from the region actually providing observational information to other regions which are not. This modeling approach, described in Section 5, will reveal the degree of uncertainty in the $O^+$ number density at a given altitude, arising from the loss of information that is being transferred along the line of sight.

## 2.3. Estimation of O II 834 Å Limb Intensities

The $O^+$ ion is the dominant ion in the F layer of the ionosphere, and assuming charge neutrality, knowledge of the $O^+$ distribution there constitutes knowledge of the electron number density there as well. Meier [1991] has discussed the contribution of O II 834 Å emissions to the airglow in the upper atmosphere and the relationship of $O^+$ to the ionosphere and magnetosphere, including experimental measurements. According to that assessment, 834 Å emissions can be moderately optically thick, primarily due to resonant scattering by $O^+$ of photons originally produced below 200 km by photoionization and photoelectron impact ionization of atomic oxygen. Link et al. [1994] have discussed laboratory measurements of cross sections for O II 834 Å production, resonant scattering, and absorption and have related the results to the airglow. We have incorporated those results into our forward model for predicting limb intensities. Under the conditions used in our tests (Section 3) and for a Chapman layer with $[N_{max}, z_{max}, H] = [1.0 \times 10^6 \text{ cm}^{-3}, 350 \text{ km}, 60 \text{ km}]$, the maximum vertical optical depth for resonant scattering of the 834.47 Å line is approximately 4.2 ($z \approx 216$ km). The corresponding vertical optical depth for pure absorption (photon loss through absorption by N2, O2, and O) is approximately 0.22.

Photoionization by solar EUV photons is the dominant production mechanism for O II 834 Å photons while the photoelectron impact ionization source contributes only about 5% of the photons. One should note that older values of cross sections used in earlier studies [Anderson

and Meier, 1985; McCoy et al., 1985] had given photoelectrons a more significant role. The present calculations include the source due to production of 834 Å photons by photoelectron impact ionization, since we use the PEGFAC code, which automatically incorporates that effect. Another minor contributor to the photon source is the resonant scattering of solar 834 Å emissions; for our limb-viewing geometry, this is a small effect (a few percent of the volume emission rate, $j_0$, for altitudes near $z_{max}$) [Meier, 1991]. As in the tests of McCoy et al. [1985] and Anderson and Meier [1985], our forward model does not include the effects of resonant scattering of sunlight. Actually, the initial source due to solar 834 Å emissions closely tracks the $O^+$ number density distribution and tends to enhance the retrieval accuracy. Omitting this factor, therefore, renders our estimates of performance somewhat more conservative. Of course, for optimal accuracy in the retrieval of parameter values from real data, the calculation will include this source.

The forward model specifies a discrete grid of altitudes $z_i$ on which to solve an integral equation for the volume excitation rate $j_k$ of line k of the triplet [Anderson and Meier, 1985; Meier, 1991]:

$$j_k(z) = j_{0k}(z) + \sigma_{0k} N_{O^+}(z) \int_{z_0}^{\infty} j_k(z') H\left(\left|\tau_k' - \tau_k\right|, \left|t_k' - t_k\right|\right) dz' \quad , \tag{10}$$

where the first term on the right-hand side (RHS) is the initial photon production term, provided by PEGFAC. The second term accounts for propagation of photons from other altitudes to a given altitude z and includes the effects of multiple resonant scattering by $O^+$. In Equation (10), $z_0$ is the altitude below which either the initial photon source term is negligible or extinction is large; $\sigma_{0k}$ is the resonant scattering line-center cross section for line k; $\tau_k(z)$ is the vertical resonant scattering line-center optical depth at altitude z ; $t_k(z)$ is the vertical pure absorption optical depth, corresponding to absorption by $N_2$ , O , and $O_2$; and H is the transport kernel [Strickland and Donahue, 1970]. The kernel H, also known the Holstein probability function, is proportional to the probability that a photon will propagate from the region (z', z'+dz') to the region (z, z+dz), undergoing resonant scattering at that point [Holstein, 1947]. Equation (10) assumes isotropic, conservative scattering and complete frequency redistribution in a plane parallel atmosphere.

Given the volume excitation rate, we can then perform an integration along the line of sight to predict the column emission rate $4\pi I$ of the radiation field in Rayleighs, as measured at the satellite [Anderson and Meier, 1985; Meier, 1991]:

$$4\pi I(\mathbf{r}, \hat{\mathbf{e}}) = 10^{-6} \int \sum_k j_k(\mathbf{r}'(s)) T_k(\mathbf{r}', \mathbf{r}) \, ds \quad . \tag{11}$$

In Equation (11), I is the radiance in megaphoton $cm^{-2} s^{-1} ster^{-1}$; $T_k$ is the probability that a photon traveling along the line of site $\hat{\mathbf{e}}$ from $\mathbf{r}'$ will arrive at $\mathbf{r}$, which in this case is the location

of the observing instrument. The spectral line shape, assumed here to be Gaussian, enters Equations (10) and (11) implicitly through the integrals for H and T, respectively. The model parameters which define the $O^+$ number density enter the forward model explicitly in Equation (10) and implicitly in both equations through the resonant scattering optical depth. Thus the values of the column emission rate on the specified grid of tangent altitudes (or OZAs) correspond to the model data vector **d** in Equation (2). Similarly, the integral on the RHS of Equation (11) corresponds to the vector function **G(m)**, unless we add a parameter $m_4$ to scale the forward model intensity estimates. In this latter case, for the $i^{th}$ line of sight vector, $\hat{e}_i$, $G_i = m_4 \times$ RHS of Equation (11). Section 6.3 previews our results when we retrieve the parameter $m_4$ along with the Chapman parameters . The solution of Equation (10) is the key factor in the integrand of Equation (11) and therefore constitutes part of the forward model. The Appendix summarizes the numerical approach to solving Equations (10) and (11).

### 3. Model System and Simulated Observations for Tests

For the purpose of determining the potential capabilities of the DIT inversion technique, we assume that the airglow is observed by an instrument on a satellite at an altitude of 850 km. The systems of interest (e.g., RAIDS) scan the limb from $10°$ to $26.5°$ below the horizon, so that the tangent altitude varies between 740 and 90 km, respectively. If the spacecraft were stationary, the distance of the tangent point from the satellite would vary from 1200 to 3200 km, respectively. To compensate for this as much as possible in the observing scheme, the systems either scan downward, if facing aft of the spacecraft, or upward, if facing forward, in order to achieve a tangent point trajectory which is as nearly perpendicular to the surface of the Earth as possible. Our tests implicitly assume that the F region is approximately uniform over the latitudinal coverage of a scan. Section 6 discusses this approximation in the context of future plans to account for latitudinal variation of the contribution function in Equation (11).

As our baseline case for computing synthetic observational data (synonymous with "observations" for the remainder of the paper), we have represented the "true" $O^+$ number density distribution as a Chapman layer with $[N_{max}, z_{max}, H] = [1.0 \times 10^6 \text{ cm}^{-3}, 350 \text{ km}, 60 \text{ km}]$. However, we have run rather extensive tests with synthetic data covering wide ranges of values for the Chapman parameters and will report on them as needed in the subsequent sections. The neutral atmosphere is always the same in our tests, given by MSIS-86 [Hedin, 1987] for the parameters shown in Table 1. In the table, "SZA" denotes the solar zenith angle, $F_{10.7}$ is the value of solar 10.7 cm flux on the previous day, and $\langle F_{10.7} \rangle$ is the 81-day average value of the flux. For these parameters, the exospheric temperature is 1200 K , which we have used in computing our resonant scattering cross sections. The latitude and longitude correspond to the tangent point whose tangent altitude is nearest $z_{max}$ .

**Table 1. MSIS Parameters for Tests**

| Year | Day | UT (s) | $A_p$ | SZA | $F_{10.7}$ | $\langle F_{10.7} \rangle$ | Latitude | Longitude |
|------|-----|--------|-------|-------|------------|----------------------------|----------|-----------|
| 1980 | 81 | 61440 | 18 | 43.49 | 188 | 163 | 32 | 254 |

To represent noise in the observations, we have converted the column emission rate in Equation (11) from Rayleighs (R) to counts using the sensitivity of 1 count $R^{-1} s^{-1}$, which is representative for the various instruments to be flown (RAIDS: 0.6 count $R^{-1} s^{-1}$ [Christensen et al., 1993]; LORAAS (ARGOS), SSULI: 1.6 count $R^{-1} s^{-1}$ [McCoy et al., 1994b]). By assumption, the observation sample interval is 1 s. We have then generated Gaussian random numbers of characteristic width $(1\sigma)$ equal to $(\text{counts})^{1/2}$, converted the numbers to Rayleighs, and added the numbers to the column emission rates derived from Equation (11).

The altitude grid for the calculation of volume excitation rates consists of 75 grid points covering the altitude range from 90 to 990 km. In the direction of increasing altitude, the locations of successive grid points increase exponentially by a constant factor. The OZA grid for computing limb intensity profiles consists of 30 points at a spacing of $0.28°$, beginning at $10.28°$

below the horizontal, and continuing with 60 points at a spacing of 0.135° at the lower tangent altitudes. This corresponds to the SSULI limb scan [McCoy et al., 1994b].

## 4. Retrieval of Chapman Parameters

This section describes the results of extensive tests that we have performed on O II 834 Å DIT inversion algorithms. For ease of presentation, we introduce the term "ideal" forward model to signify a forward model which satisfies the following: (1) the model depends on no approximate or unknown physical quantities other than the model parameters defining the retrieved number density profile and (2) the parameterization of the retrieved number density profile matches the functional form describing the set of ground truth profiles. By definition, the values of the remaining physical parameters in the "ideal" forward model are identical to the true values characterizing the system being measured. In the limit of negligible statistical noise, the intensity calculated with the ideal forward model represents an optimal fit to the intensity data when the ground truth number density profile is entered into the forward model. A model that is not ideal could, for example, use an incorrect instrument sensitivity factor so that, given a ground truth number density profile, the model would actually predict intensity values that were low or high by a constant factor.

To determine an upper limit to the potential of the DIT inversion techniques and to provide a baseline for subsequent refinement of the DIT algorithms, the tests presented in Subsections 4.1-4.3 assume that the forward model is, in fact, ideal. Since the Chapman layer representation of the ion number density profile is being used, the length of the model parameter vector **m** is $M = 3$. Section 4.4 discusses the uncertainties in *a priori* inputs to the forward model in realistic, nonideal cases.

### 4.1. Typical Results for the Three-Parameter Model

Figure 1 shows typical results for our tests of the three-parameter model. The results of each test appear in two diagrams:
(1)    the retrieved (DIT) $O^+$ number density versus altitude (solid line), along with error bars derived from Equation (9) for propagation of errors, and
(2)    synthetic intensity data (centers of short vertical lines) with horizontal $\pm\sqrt{N}$ error bars and the DIT fit (solid line).

In both cases, the "true" values of [$N_{max}$, H] were the baseline values, [$1.0 \times 10^6$ cm$^{-3}$, 60 km]. For panels 1a and b, $z_{max}$ was 250 km, and for panels 1c and d, $z_{max}$ was 350 km. Each calculation used a different set of random numbers to simulate noise. In both cases, the initial parameter estimates used to start the DIT iteration process were 20% above the "true" values.

Comparing the information in the plots and the figure caption for the two cases, we see that the uncertainties in the retrieved values of $N_{max}$ and $z_{max}$ are significantly larger when the true $z_{max}$ is 250 km and that the uncertainties drop to minimal values when $z_{max}$ increases to 350 km. On the other hand, the uncertainty in the scale height parameter is small in both cases (see figure caption). Section 4.3 interprets these observations physically and reveals their respective levels of generality by studying the uncertainties in the retrieved parameters as functions of the ground truth parameter values. The first figure, however, does support the assertion that significant information on the Chapman parameters can be retrieved from O II 834

Å limb intensity measurements, at least when the ion distribution in the F region follows Equation (1).

## 4.2. Convergence Properties

The nonlinearity of the intensity calculation in the forward model naturally requires that the solution space be searched for the optimal $O^+$ number density profile. The simplest and often the most cost-effective search procedure involves iteration from an initial estimate of the model parameters. We have adopted this approach and have thoroughly tested the sensitivity of the retrieved parameters to the initial estimates of their values. We began by creating synthetic data for the baseline model [$1 \times 10^6$ cm$^{-3}$, 350 km, 60 km] with Gaussian noise superimposed. We found that the same values of the retrieved parameters were obtained independent of the initial estimates. We have duplicated these tests for a large number of synthetic data sets based on a wide range of ground truth Chapman parameters (ranges shown in Figure 3). In all cases, we have obtained results that were independent of the initial estimates used to start the DIT calculation. This satisfies the important condition of robustness against choice of initial parameters. For a given limb scan, the method also converges to a "unique" maximum likelihood solution. Here the term "unique" means that the retrieved parameters have identical significant figures and magnitude.

The next test involves using the same baseline parameters for the synthetic data, but superimposing different Gaussian noise on the synthetic data for each initial estimate of the parameters. This time the retrieved parameters are different for each initial guess, due to the dependence on the Gaussian noise, i.e., the maximum likelihood solution changes. The results are summarized in Table 2, which lists four initial estimates of the parameters and the percentage differences of the retrieved parameter values from the "true" values. Beneath the table appear the "true" parameter values used to generate the synthetic data and the maximum $1\sigma$ uncertainties obtained from the covariance matrix. Ordinarily, to compute the approximate $1\sigma$ values, one would have to perform these tests with a large number of synthetic limb scans, each with different simulated noise. The standard deviations of the retrieved parameter values would then follow from the averages of the squares of the respective | True - DIT | values. Instead we have used Equation (7) for the covariance matrix, [**cov m**$^e$].

**Table 2.** Convergence Test Results for Three Parameter Model*

| Case | Initial Guess † | | | Convergence | ǀTrue - DITǀ, % | | |
|------|-------------------|-----------|-----|-------------|-----------------|-----------|-----|
|      | $N_{max}$ | $z_{max}$ | H | steps | $N_{max}$ | $z_{max}$ | H |
| 1 | 10.0 | 600 | 120 | 27 | 4.4 | 0.8 | 1.1 |
| 2 | 2.0 | 600 | 120 | 8 | 2.3 | 0.9 | 0.0 |
| 3 | 1.5 | 525 | 90 | 7 | 3.7 | 1.8 | 0.2 |
| 4 | 0.5 | 250 | 30 | 6 | 0.9 | 0.2 | 0.1 |

\* The ground truth values [ $N_{max}$, $z_{max}$, H] are [ $10^6$ cm$^{-3}$, 350 km , 60 km], and maximum $1\sigma$ values are [ 6.0 %, 2.7 %, 1.7 %). Different noise was used for each run.

† The units for $N_{max}$ are $10^6$ cm$^{-3}$, and the units for both $z_{max}$ and H are km.

Figure 2 corresponds to initial estimates 1 and 4 in Table 2. The shape of the initial estimates for the intensity profile are quite different for the two cases, as expected from the work of McCoy et al. [1985]. At convergence, the retrieved intensity and ion number density profiles are in excellent agreement with the true profiles in all cases. The $1\sigma$ uncertainties are consistent with that picture. We have duplicated the above tests for a large number of synthetic data sets based on a wide range of ground truth Chapman parameters. In all cases, we have obtained results similar to those in Table 2 and Figure 2. Thus we conclude that convergence is excellent and consistent with the expected uncertainties in the DIT result.

While our results are quite encouraging, we reiterate that we are treating an ideal situation in which the same forward intensity model and the same functional form for the O$^+$ number density distribution are used to generate both synthetic data and DIT estimates. The addition of random numbers to simulate noise in the data tends to mitigate this somewhat, since the smooth forward model estimates cannot match the synthetic data exactly. In a future paper, we will explore the potentially more difficult situation in which the representation of the ion number density distribution used to generate synthetic data is different from that used in the DIT forward model.

### 4.3. Uncertainties in Retrieved Model Parameters

As indicated earlier, the standard deviation $\sigma_i = ([\mathbf{cov\ m^e}]_{ii})^{1/2}$ provides a useful measure of the uncertainties in the $i$th retrieved model parameter. To generate approximate values of $\sigma_i$, we compute the forward model intensity gradient vector, $\nabla \mathbf{G}$ , at the location of the "true" solution in model parameter space. This gradient vector consists of the usual one-sided numerical derivatives. We then use $\nabla \mathbf{G}$ to evaluate Equation (7) for [$\mathbf{cov\ m^e}$] , of which $\sigma_i^2$ are the diagonal elements. We have performed this procedure over a three-dimensional grid of "true" Chapman parameter values. Note that the results described below apply only to limb scans from an altitude of 850 km and covering OZA between 100° and 116.5°.

14

Figure 3 shows two-dimensional contour plots depicting the dependence of each $\sigma_i$ on the "true" Chapman parameters underlying the observations. We have selected only a subset of two-dimensional planes within the three-dimensional grid of "true" values ("ionospheric states"). Over each plane, one Chapman parameter remains fixed while the others vary. We have chosen to fix $N_{max}$ at $1 \times 10^6 cm^{-3}$ and H at 60 km, both baseline values, while the fixed value for $z_{max}$ is 250 km, chosen because of the interesting structure near that value. Higher values of "true" $z_{max}$ show parameter uncertainties with progressively less structure and decreasing uncertainty values. As an example of the use of Figure 3, the percentage uncertainty in the retrieved $N_{max}$ for the baseline "true" ionospheric state appears in Figure 3(a) or Figure 3(c) as approximately 5%.

The behavior of the uncertainty in the retrieved Chapman parameters, as seen in Figure 3, follows from Equations (1), (10), and (11). Equation (11) shows that the behavior is the result of the interplay among the line-of-sight path length, the enhancement of the volume excitation rate as resonant scattering increases with the $O^+$ number density in the F region, and the reduction in the 834 Å signal through self-absorption and pure absorption, as represented by the transmission function T in Equation (11). The dependence of the volume excitation rate and transmission factor on $O^+$ number density have opposing effects on the intensity, and local extrema in the uncertainty could easily occur as the true $N_{max}$ varies. The value of $z_{max}$ directly determines the altitudes at which resonant scattering becomes appreciable and strongly affects the transmission factor linking the F region with the satellite. The scale height affects the shape of topside limb intensity profile and the column density. The latter, in turn, affects the optical depth entering T. The transmission function itself can be a significant source of information on the values of the Chapman parameters.

The remainder of this subsection uses such interpretations of Equation (11) to reveal qualitative aspects of the dependence of the uncertainty in retrieved Chapman parameters on the true values underlying the data. Because the interplay among the factors in Equation (11) is extremely complex and because space is limited, a discussion of structural details of the contour plots of uncertainty is beyond the scope of this paper. The most important message of Figure 3 is that the uncertainty is small or moderate over a significant region of parameter space. The potential of the 834 Å DIT retrieval algorithms is, therefore, considerable.

### 4.3.1. Uncertainty in Retrieved $N_{max}$

The first three contour plots in Figure 3 show the behavior of $\sigma(N_{max})$. In Figure 3a, for which the true values of $N_{max}$ and $z_{max}$ vary and the true value of H is 60 km, the uncertainty in retrieved $N_{max}$ is largest for low values of $z_{max}$, dropping off quickly with increasing $z_{max}$. As $z_{max}$ increases, the distance along the line of sight from the observer to the tangent point at $z_{max}$ decreases. As a consequence, the optical path length to the region of the peak density drops off rapidly, permitting more information (i.e., photons) to reach the sensor. At lower values of $z_{max}$, pure absorption becomes appreciable and can mask information coming from the F-layer. Hence, the lower the ionosphere, the greater is the uncertainty in $N_{max}$.

The region of uncertainty values > 5% in Figure 3a extends to higher true $z_{max}$ as $N_{max}$ increases. In that region, the contours indicate a plateau with a modest undulation. On the other

hand, the uncertainty is below 5% over much of the diagram. Upon inspecting similar plots for true H between 30 and 90 km, we have found the same qualitative situation although the peak uncertainty is larger at the two extremes than in the 40 - 80 km range. Also, as H increases, the region of uncertainty values > 5% moves toward higher $z_{max}$ . When $N_{max}$ and H are large, resonant scattering plays a significant role not only in enhancing the volume excitation rate but also in reducing the magnitude of the transmission function. Figure 3a and its relatives at different values of H indicate that, as $N_{max}$ and H increase, the inhibition of photon transmission to the observer is the greater effect, reducing information received and increasing uncertainty in the retrieved parameters.

Figure 3b shows the uncertainty in the retrieved value of $N_{max}$ as a function of the true values of $N_{max}$ and H when the true $z_{max}$ = 250 km, at which the uncertainty is greatest. The diagram shows that, for this low peak height, the uncertainty tends to be greater at larger values of H for a given $N_{max}$ . For a given value of H, the uncertainty peaks in the vicinity of $N_{max}$ = 5 $\times 10^5$ . On the other hand, similar plots for $z_{max} \geq 300$ km show the trend of the previous paragraph: the peak uncertainty occurs in the upper right corner of the $[N_{max}, H]$ plane and the peak value decreases with increasing $z_{max}$. Figure 3c and its higher $N_{max}$ relatives are consistent with this picture.

## 4.3.2. Uncertainty in Retrieved $z_{max}$

Figures 3d, e, and f show the plots of $\sigma(z_{max})$ corresponding parametrically to those of $\sigma(N_{max})$ in Figures 3a, b, and c, respectively. The morphologies of the $\sigma(z_{max})$ and $\sigma(N_{max})$ contour diagrams are similar. Figure 3d shows variations with true $N_{max}$ and $z_{max}$ for true H = 60 km. For a given value of H, the error in $z_{max}$ peaks in approximately the same region of the $[N_{max}, z_{max}]$ plane as that for $N_{max}$ , although the region of high uncertainty does not extend as far up the $N_{max}$ axis. In addition, as H varies from 30 to 90 km, the behavior is also similar to that of $\sigma(N_{max})$. Figures 3e and 3f confirm this picture, showing the same qualitative behavior as those for $\sigma(N_{max})$. The marked qualitative similarities between $z_{max}$ and $N_{max}$ occur because both parameters describe the peak in $O^+$ number density profile, and both relate monotonically to the optical path length between the detector and the region of the peak in the ion number density profile. Plots of two-dimensional confidence regions in $[N_{max}, z_{max}]$ space confirm that $N_{max}$ and $z_{max}$ are highly correlated [Picone et al., 1994, 1995b; Kelley et al., 1994]. The most notable difference in $\sigma(z_{max})$ and $\sigma(N_{max})$ is that the uncertainty in $z_{max}$ at a given point is smaller than that of $N_{max}$. This is due to the close relationship between $z_{max}$ and the altitude of the peak in the limb intensity profile over a wide range of ionospheric parameter values.

## 4.3.3. Uncertainty in Retrieved Scale Height

The behavior of $\sigma(H)$, exemplified by Figures 3g, h, and i, is qualitatively different from that of the other two parameters, as shown by a visual comparison of corresponding diagrams. Unlike $z_{max}$ and $N_{max}$ , which are related primarily to the altitude and magnitude of the peak intensity, the scale height determines the shape of the normalized $O^+$ number density profile and thus, the shape of the topside limb intensity profile. The contour diagrams in Figure 3 and their relatives show the uncertainty in H to be quite low over the entire parameter space. This is

16

primarily because the observations need not sample far into the medium to obtain H. Within the context of these small uncertainties, the diagrams indicate that the uncertainty in H varies inversely with that of $N_{max}$ and $z_{max}$. For large true $N_{max}$ and $z_{max}$, the uncertainty in retrieved H will decrease if the minimum OZA of the limb scan is reduced or if the observation altitude is increased.

4.4. Uncertainties in Other Components of the Forward Model

Uncertainty in the forward model can arise from several sources; examples are numerical procedures, instrument calibration, estimates of the solar EUV irradiance, and cross sections, including those for photoionization, photoelectron impact ionization, resonant scattering of photons by ions, and absorption of photons by neutral species. The Appendix provides the details of our numerical procedures. The physical quantities mentioned as examples appear as *a priori* parameters which presently do not vary during the retrieval process. A detailed study of methods to compensate for errors in these parameters and perhaps to retrieve them from the intensity data is beyond the scope of this paper. We can, however, offer a few observations on this topic.

First, we can retrieve a data scaling model parameter $m_4$ to address any errors which have the effect of scaling of the intensity by a factor that is approximately uniform in altitude. This is the case if the assumed instrument sensitivity is in error, or if an approximately altitude-independent scaling error exists in the g-factor for photon production, or if some combination of the two occurs. Since photoionization of atomic oxygen is dominant, a uniform error in the magnitude of the associated cross section should appear as an approximately uniform scaling error in the 834 Å g-factor. A subsequent paper [Picone et al., 1995a] deals with such situations; Section 6 previews our results.

The influence of the various pure absorption cross sections requires a separate investigation. An inspection of Equation (10), however, allows us to determine the ability to use additional parameters to compensate for errors in the resonant scattering cross sections. Notice the product of the line center resonant scattering cross section $\sigma_{0k}$ and $N_{max}$ preceding the integral. The only other factor containing $\sigma_{0k}$ is the resonant scattering optical depth $\tau_k$, which is proportional to $\sigma_{0k} \times N_{max}$. This means that any model parameter scaling $\sigma_{0k}$ can be absorbed into the model parameter $N_{max}$. No method, therefore, can retrieve both types of parameters uniquely from O II 834 Å intensity data alone. If we have additional coincident data, such as F region electron density profiles measured by incoherent scatter radar, and if we have the data in sufficient quantity, we should be able to calibrate the DIT-retrieved value of $N_{max}$. We could then derive a correction factor for $\langle \sigma_{0k} \rangle$, where the brackets indicate an average over the lines in the triplet, or we could derive correction factors for the individual $\sigma_{0k}$, if the observations resolve the 834 Å multiplet components. One should note that the resonant scattering cross sections for O II 834 Å emissions are known to within 10% (Ho and Henry, 1983).

17

## 5. Concentration Scalar Model

The previous section discusses uncertainties in the retrieved Chapman parameters as functions of the "true" state of the ionosphere (i.e., the "true" parameter values). The desired uncertainties are often those of the number density at various altitudes within the F-region, as retrieved from a given limb intensity data set. Because of resonant scattering and pure absorption, the densities at lower altitudes might not contribute significantly to limb intensity data that correspond to lower tangent heights. The propagation of errors formula in Equation (9) assumes that the low altitude extrapolation provided by the Chapman layer is correct.

At the suggestion of R. Thomas [private communication, 1993], Meier and Picone [1994] introduced the concentration scalar model (CSM) to determine more directly which portions of the atmosphere actually contribute to the information received by a UV sensor viewing the limb from a satellite. In the CSM, the model parameters are the values of the ion number density at the various altitudes on a grid. Unlike the Chapman layer model of Equation (1), the model parameters of the CSM are not coupled through a constraining functional form. As a consequence, the retrieval process must allow for the possibility that the data are not sensitive to densities at some altitudes; for example, this could be caused by extinction at the lower altitudes. We must, therefore, input *a priori* values of the number density and the corresponding uncertainty (variance) at the various grid points. For any grid points from which a negligible number of photons reach the sensor, the DIT code will return the respective *a priori* values of the number density. Similarly, [**cov m**$^e$], the covariance of the retrieved model parameters, reverts to [**cov m**], the *a priori* covariance, at those grid points. At other points, from which appreciable information reaches the sensor, the variances of the retrieved density values will be smaller than those of the *a priori* values. This improvement arises from the added information provided by the data, as shown by the first term on the RHS of Equation (7). On the other hand, Equation (6) shows that, if the data are sufficiently noisy (large variances) or if the *a priori* parameter values are known with sufficient accuracy (small variances), then the data will contribute little to the "retrieved" density values.

Our primary goals in using the CSM in the present paper are to determine those altitudes from which appreciable amounts of information reach the sensor and to assess the relative importance of each altitude region as compared to others. Thus, we require only approximate, relative values of the variances, $\sigma_i^2$ , of the model parameters (O$^+$ number densities), where the index $i$ runs over the altitude grid. Our "standard" or baseline case for computing synthetic observational data is again a Chapman layer with [$N_{max}$ , $z_{max}$ , H] = [$1.0 \times 10^6$ cm$^{-3}$, 350 km, 60 km]. The number of parameters equals the number of points on the altitude grid, i.e., $M = 75$.

To obtain the relative variances, we use the same technique as in Section 4.3 . First, we compute the forward model intensity gradient vector, $\nabla$**G** , at the location of the "true" solution in model parameter space. Here the gradient vector consists of the usual one-sided numerical derivatives. We then use $\nabla$**G** to evaluate Equation (7) for [**cov m**$^e$], of which $\sigma_i^2$ are the diagonal elements. For the CSM, Equation (7) requires a covariance matrix, [**cov m**], for *a priori* model parameter values. In this case, [**cov m**] merely provides an upper bound on our relative

variances and is somewhat arbitrary. For the present tests, we have assigned an upper bound of 20% to the uncertainties of the *a priori* model parameter values. Because the concentrations at the various altitudes are independent of each other, [cov m] is diagonal, with element $ij$ is given by $\delta_{ij} [0.2 \ N_{O^+}(z_i)]^2$. The symbol $\delta_{ij}$ is the Kronecker delta.

Figure 4 shows typical plots of the standard deviation of the retrieved number density values, using [cov $m^e$] computed from the CSM. The individual panels correspond to different values of the "true" Chapman parameters from which the synthetic data were generated. Appearing above panels (b)-(f) are the "true" parameter values which differed from the baseline values when the respective synthetic limb intensity profiles were generated. The figure shows that, with the exception of very low Chapman layers (true $z_{max}$ = 250 km), altitudes somewhat below the true $z_{max}$ and higher contribute appreciable information for determining the optimum result. The cases with higher and lower $N_{max}$ are quite similar to the baseline case while an extremely low value of H shows stronger dependence on altitudes near $z_{max}$.

Also shown in Figure 4 are the uncertainties computed from Equation (9) for the three-parameter forward model. The Chapman layer parameterization permits more accurate retrieval of the ion density profile, which we expect, since our "observational data" are derived from a Chapman layer representation of the ionosphere. In addition, the small number of Chapman parameters and the dependence of the density at each altitude on all three parameters mean that the Chapman parameters can be evaluated without sampling the lower altitudes.

19

## 6. Summary and Discussion: Practical Applications

Our purpose in this paper has been to demonstrate the potential capability and structure of algorithms based on discrete inverse theory for retrieving the distribution of $O^+$ in the dayside F layer of the ionosphere from the O II 834 Å airglow. Our immediate application is to satellite-based observations by a limb-scanning EUV spectrograph. The main question regarding this problem concerns the ability to acquire sufficient information on the $O^+$ distribution from the O II 834 Å emissions, which are moderately optically thick due to resonant scattering within the F layer. The optical path length along the line of sight can be quite large when viewing the limb of the Earth, preventing photons originating in the lower thermosphere from reaching the observing system. To test the potential capability of the method we have used the three-parameter Chapman layer representation of the $O^+$ distribution and a robust forward model for computing the limb intensity, including the effects of resonant scattering by $O^+$ and pure absorption by the major neutral species.

In this paper, we have treated only the "ideal" case. In the ideal case, the forward model is "exact," containing all of the physics necessary to represent $O^+$ distributions in the F region and to compute accurate limb intensity profiles, excluding statistical noise. Hence, our results for the ideal case represent an approximate upper bound on the capability that we seek to develop. For "nonideal" cases, the DIT forward model differs materially from "reality," as represented in this case by the model used to generate "observations." For example, the values of key cross sections used in the forward model have an associated measurement uncertainty. Alternatively, the analytic representation of the $O^+$ number density distribution in the retrieval code might not be identical with the functional form of the ground truth distribution. Section 6.3 below previews recent results on our approach to a particular nonideal case.

Our tests have shown that the three-parameter forward model always converges to a unique maximum likelihood solution from a variety of initial estimates of the Chapman parameters, even when the initial peak ion number density is an order of magnitude too large and the other two parameters are high by a factor of two. We have mapped the uncertainty in each parameter over the three-dimensional space covered by wide ranges of true parameter values. Clearly some ionospheric states are more accurately retrievable than others.

The concentration scalar model has provided a more exact picture of the region of the ionosphere being probed by the limb-scanning measurements. The CSM shows that information on the ion number density profile is available over the entire top side down to the peak, and usually somewhat lower. This result gives us confidence in the viability of the DIT technique for deriving information on the F region of the ionosphere from 834 Å limb scans. Although our tests have been specific to a single set of parameters for satellite-borne limb scanning, we expect the results to apply to a range of satellite altitudes and orbits. In fact, the basic elements of the retrieval algorithms also apply to measurements from sounding rockets [Dymond et al., 1995]. Coincident ionosonde measurements have verified the $O^+$ number density retrieved by Dymond et al., indicating that the present paper provides a strong foundation for practical, robust methods. In the following subsections, we mention some of the issues which will be addressed in future publications.

## 6.1. Assumptions Regarding the Observations and the Ionosphere

First we consider factors related to the design of the observing system. Equation (11) shows that we have not included the finite field of view of the sensor in our intensity integral; theoretically we would have to average over a range of lines of sight. Our present tests therefore include an implicit assumption of uniformity across the sensor field of view. For the satellite-borne, limb-scanning systems mentioned earlier, the vertical field of view is approximately $0.1°$ and is small enough that our results are not severely impacted by this approximation. Pointing accuracy will also affect the accuracy of the retrieval process. If the look angle is off by $0.1°$, the minimum tangent height could be off by approximately 5 km. The retrieved altitude of the peak $O^+$ density could be off by a similar amount. The formalism of Section 2 for handling inaccuracies in the forward model will allow us to investigate this aspect.

We have treated the distributions of ions and neutrals as uniform over the latitude range covered during a scan. For the 834 Å triplet, which can be moderately optically thick, this is a better approximation than for an optically thin emission because a significant amount of information propagating from the distant latitudes can be scattered out of the line of sight. On the other hand, this aspect should be straightforward to handle in the DIT framework by including a latitudinal parameterization.

Presently we evaluate the distributions of the major neutral constituents using the MSIS-86 model [Hedin, 1987]. In practice, for RAIDS, ARGOS, and SSULI, we could use the results of the DIT algorithm for extracting such information from FUV limb intensity measurements [Meier and Picone, 1994]. More generally we might combine the EUV and FUV data sets to extract ion and neutral number density profiles simultaneously, although the practical advantages of such an approach have not been analyzed.

Anderson et al. [1987] have indicated that the simple Chapman layer used here is not a sufficiently robust parameterization of the ion distribution produced by realistic numerical simulations and perhaps the actual F region. D. N. Anderson and M. Fox [private communication, 1993] have instead proposed more general forms in which the model $O^+$ profile contains "topside" and "bottom-side" parameters; the scale heights might also be linearly dependent on altitude. The total number of parameters would then vary between $M = 5$ and 7. We are currently testing such representations against synthetic data based on empirical databases and models.

## 6.2. Numerical Procedures and Solution Criteria

A practical algorithm must consistently converge to acceptably accurate representations of the $O^+$ distribution in the daytime ionosphere and must do so in an acceptably short computational time interval. We have not optimized the present algorithms and numerical procedures for high-speed processing. The factors to be considered are as follows: the accuracy of the initial estimate of parameter values, definitions of convergence criteria for the iterative

process, time constraints placed on the retrieval activity by the user and the observing system, and computer hardware.

The best method of increasing retrieval speed is to obtain a sufficiently accurate initial estimate of the parameter vector. An example of a strategy for achieving this is to use the results of previous limb scans to initialize the retrieval from a given scan. This is a sequential estimation technique proposed by Rodgers [1976] and investigated by Ortland et al. [1993]. We intend to study variations on this theme and to develop appropriate enhancements.

Regarding the termination point of the iterative process, we have been computing a maximum likelihood solution, using a generalization of the Levenberg-Marquardt procedure described in the *Numerical Recipes* series [Press et al., 1989]. Currently the process stops when the change in $\chi^2$ is smaller than a preset fractional value ($10^{-4}$). We have investigated other termination criteria but have not determined an optimal strategy. In addition, the LM method of selecting the optimal step size for each iteration can be computationally expensive, due to the calculation of numerical derivatives for the 834 Å inversion.

The optimization of computer codes also involves consideration of the requirements of the user and the user's particular computer host. For example, if a scan of the Earth's limb requires 100 s and if each dayside scan is to be processed for a timely assessment of "ionospheric weather," the reformatting and calibration of raw data, retrieval of $O^+$ distributions, production of routine data products, and delivery to the user must require less than 200 s per scan. (The 200 s time interval derives from the fact that only dayside retrievals are being considered.) Otherwise the data processing activity will fall behind the rate at which new data arrive. In addition to the computational complexity of the algorithms, the speed of computer hardware and the optimization of computer codes that implement the algorithms are critical elements in achieving an adequate duty cycle.

Most importantly, better criteria might exist for defining the DIT solution than that of the maximum likelihood. For the retrieval of a three-parameter Chapman layer from a given limb intensity profile, the DIT procedure converges arbitrarily close to a unique maximum likelihood solution. For some ionospheric states, however, the maximum likelihood solution itself can change by a significant amount as the particular realization of statistical noise changes. In preliminary tests, we have had some success in finding a different criterion for defining the DIT solution so that the solution varies less strongly with the particular sample of noise. This issue merits a careful and detailed study.

6.3. Advanced Topics

We conclude with a preview of results on two topics that extend beyond the present baseline study. While we will be reporting in detail on these topics in succeeding publications [Picone et al., 1995a,b], interest has been sufficiently high to warrant mention here.

### 6.3.1. Different Chapman Layers With "Nearly Identical" Intensity Profiles

Link et al. (1994) have computed model 834 Å limb intensity profiles for a satellite in an 850 km orbit while viewing (model) ionospheres with values of $N_{max}$ differing by a factor of 2 and $z_{max}$ differing by 50 km. Excluding the effects of noise, such limb intensity profiles can differ by approximately 3% or less at look angles corresponding to tangent altitudes below 650 km. Given that this difference is much less than the scatter seen in data from the STP78-1 mission [McCoy et al., 1985], Link et al. conclude that, for STP78-1 data, the uncertainties in $N_{max}$ and $z_{max}$ for the retrieved $O^+$ number density profiles can be worse than the respective factors of 2 and 50 km by which the model ionospheres differ.

Presently we are studying the statistical uncertainty in the retrieved parameters in the context of future EUV remote sensing missions, for which the instruments are more sensitive than that of STP78-1 by a factor of three (RAIDS) or more (SSULI, ARGOS). In contrast to the procedure of Link et al., which was based on inspection, the DIT approach provides an analytic method, Equation (7), for estimating the uncertainties in the retrieved profiles. In addition, the minimization of a characteristic function (like $\chi^2$) provides the basis for selecting an optimal set of model parameters, thereby distinguishing among various "nearly identical" model intensity profiles and their underlying $O^+$ number density profiles. This discrimination is statistical because, for a given "true" ionospheric state, the retrieved parameter values vary with the particular realization of statistical noise present in a given limb intensity profile. The statistical spreads in retrieved parameter values, therefore, depend on the sensitivity of the observing instrument.

To verify this capability, we have studied two different cases which are similar to the single case shown by Link et al. Each test case consists of two "true" ionospheric states with significantly different values of $N_{max}$ and $z_{max}$ but with "nearly identical" intensity profiles, excluding statistical noise. To each intensity profile in a pair, we added twenty different sets of random noise, generating forty synthetic limb intensity observations per pair of intensity profiles; we did this for each of three instrument sensitivities: 0.2, 0.6, and 1.0 counts/R/s. We then retrieved the maximum likelihood solution for each limb observation. Our results are as follows:

(1) Compared to the case of low sensitivity instruments like that on STP78-1, the uncertainties in the retrieved parameters are much lower for the more sensitive instruments aboard future missions. The scatter in the noise is much lower, and hence, the ability to resolve "nearly identical" limb intensity profiles is significantly greater.

(2) The cases in which significantly different Chapman layers yield nearly identical limb intensity profiles are those for which the uncertainty in the retrieved $N_{max}$ and $z_{max}$ is high. Over a great range of values for the "true" Chapman parameters, this statistical uncertainty is less than 5% (Figure 3), so that the issue of nearly identical limb intensity profiles is much less important.

(3) For future missions, the 68% confidence regions of the retrieved solutions are well separated and are readily distinguishable.

Thus, we find from this preliminary analysis that, by employing powerful inversion methods, such as DIT, remote sensing of the dayside ionosphere using O II 834 Å measurements can indeed yield reliable $O^+$ concentrations with relatively low uncertainties.

6.3.2. Retrieval of a Data Scaling Factor

For a 3-parameter representation of the $O^+$ number density profile, we have also investigated extensively the properties of an algorithm which retrieves an additional parameter, $m_4$, that scales the intensity estimate by the forward model prior to comparison with observational data [Picone et al., 1995a]. This approach can mitigate the influence of inaccurate instrument calibration, which may be attributable to errors prior to launch or to changes that occur over the course of the mission. Such inaccuracy can cause incorrect scaling of the intensity, as estimated by the forward model. Another factor which might also be mitigated in this way is an error in the magnitudes of the g-factors (excitation rate per second per ion) for production of the O II 834 Å emissions. Errors in g-factors can arise from uncertainties in the excitation cross sections and in the solar flux, the neutral atmosphere, and the photoelectron flux. The retrieval of a single data scaling parameter would be most effective when the g-factor is off by a multiplicative scalar that is approximately constant in altitude over the range of interest.

Our preliminary tests consider Chapman layers with true $[N_{max}, H] = [2.0 \times 10^6 \text{ cm}^{-3},$ 60 km] and true $z_{max} \in \{250, 350, 450, 550\}$ km. To obtain synthetic observational data for our tests, we have generated intensity values with the forward model and then, prior to adding simulated noise, we have scaled them by a factor which differed from 1.0 (either 1.3 or 0.7). For each value of the true $z_{max}$, we have used twenty different synthetic limb intensity profiles (i.e., twenty sets of random noise). Without the retrieval of the fourth model parameter, the DIT code could not obtain useful estimates of the true Chapman parameters. However, with the additional retrieved parameter, the performance is consistent with the previous sections, which have assumed the ideal case (true $m_4 = 1.0$). For $z_{max} \geq 450$ km, the average values of the retrieved Chapman parameters and the scaling factor are within a few percent of the true values, and the standard deviations are small. As the value of $z_{max}$ decreases below 450 km, the uncertainty increases as in the ideal cases treated earlier (Figure 3). Since the true value of $m_4$ is independent of the state of the local ionosphere, one has the luxury of selecting only limb intensity data which satisfy stringent requirements. Note that the systems considered here provide approximately 30 limb intensity profiles per orbit — more than enough for this purpose. Once a value for $m_4$ has been obtained, one can perform routine 3-parameter inversions with the forward model intensity scaled by that value of $m_4$. Our expectation is that this technique will work well for generalized representations of the ionosphere, for which $M > 3$. Since the calibration of the instrument might change over time, periodic updates of the value would be desirable.

## 7. Acknowledgments

## Appendix: Numerical Details of the Forward Model

We briefly describe the forward model used for these tests. The model includes the effects of multiple resonant scattering by $O^+$ and absorption of photons by O, $N_2$, and $O_2$. The integral equation (10) is identical to that discussed in the original paper on the topic by Anderson and Meier [1985]. Earlier, Strickland and Donahue [1970] and Strickland and Rees [1974] had analyzed the general problem of multiple resonant scattering under the assumption of complete frequency distribution. Anderson and Meier [1985] later modified the approach for 834 Å airglow, adding an approximate "external source" (boundary) term to Equation (10) to account for the fact that the region in which the emissions are produced can lie well below the F layer. When comparing recent calculations to those in the original work, one must remember that the accepted values of cross sections for photon production, resonant scattering, and absorption have changed as better data have become available [Link et al., 1994].

The need for the external source term in the method of Anderson and Meier arose because the problem is solved on the resonant scattering optical depth grid, which ceases significant variation with decreasing altitude once the "bottom" of the $O^+$ layer is reached. This requires the establishment of an arbitrary definition for the lower boundary of the $O^+$ layer. Since most of the photons are usually produced below the $O^+$ layer, the external source must faithfully represent propagation of the photons into the F region from below. The code used for the present work solves Equation (10) on an altitude grid that extends below the region where 834 Å photons are produced so that no boundary term is required. For this reason, no interpolation of physical quantities onto an optical depth grid is necessary, and the only other approximations are purely numerical, such as, the treatment of physical quantities as discrete.

The user can select the altitude grid, denoted by $z_i$ for $i$ ranging from 1 to N. We are presently using a grid of 75 points, the values of which increase exponentially from cell to cell; tests have shown only weak dependence on the particular gridding scheme. We evaluate the volume excitation rates at these altitude values. In the current implementation, we treat the set $\{z_i ; i = 1, 2, ... , N\}$ as the cell boundaries, with cell centers at $\{z^c_i \equiv \frac{1}{2}(z_i + z_{i+1}), i = 1, 2, ... , N-1\}$. In the following equations, the subscript i with no superscript will label a quantity which is evaluated at $z_i$, and the subscript i with superscript c will label a quantity which is evaluated at $z^c_i$. We then solve the following numerical approximation for Equation (10) at cell centers:

$$j^c_i = j^c_{0i}(z) + \sigma_0 (N_{O^+})^c_i \left\{ \sum_{m \neq i} j^c_m \left| \varepsilon\left( \left|\tau_{m+1} - \tau^c_i\right|, \left|t_{m+1} - t^c_i\right| \right) - \varepsilon\left( \left|\tau_m - \tau^c_i\right|, \left|t_m - t^c_i\right| \right) \right| \right. \\ \left. + j^c_i \left[ 2 \varepsilon(0,0) - \varepsilon\left( \left|\tau_{i+1} - \tau^c_i\right|, \left|t_{i+1} - t^c_i\right| \right) - \varepsilon\left( \left|\tau_i - \tau^c_i\right|, \left|t_i - t^c_i\right| \right) \right] \right\}$$

, (A1)

where

$$\varepsilon(a,b) \equiv \frac{1}{2\sqrt{\pi}} \int_{-\infty}^{\infty} \frac{e^{-2x^2} E_2(a\,e^{-x^2} + b)}{\sigma_0\,N_{O^+}(z_i^c)\,e^{-x^2} + \sum_{\alpha} \sigma_{\alpha} N_{\alpha}(z_i^c)}\,dx \qquad . \qquad (A2)$$

The second term on the RHS of Equations (10) and (A1) includes multiple scattering effects. In Equation (A2), the index $\alpha$ ranges over the major neutral species, which absorb the 834 Å triplet emissions. The functional $E_2$ is the second order exponential integral [Abramowitz and Stegun, 1972]. To compute $\varepsilon(a,b)$, we have used the Gauss-Hermite quadrature formula with terms up to $n = 20$ [Press, et al., 1989; Abramowitz and Stegun, 1972; Krylov, 1959].

For the purpose of testing the DIT approach, the numerical approximations have been straightforward. The following assumptions are implicit in the above equations:

(1)     the cell sizes are small enough so that the volume excitation rate is approximately constant over each cell;

(2)     the variation with altitude of both the resonant scattering and pure absorption optical depths is approximately linear about the center of each cell;

(3)     the lower bound of all frequency integrations for the Gaussian line shape can be approximated by $-\infty$ , incurring negligible errors.

To solve Equation (A1), we subtract the second term on the RHS from both sides, giving us a matrix equation, $[A]\,\mathbf{j} = \mathbf{j}_0$ . One can then use a standard matrix inversion technique to solve for the total volume excitation rate $\mathbf{j}$, which rapidly approaches $\mathbf{j}_0$ below the Chapman layer. At each look angle, we compute the intensity in Equation (11) by using a Simpson's rule integration with 60 points along the line of sight, assuming a spherical Earth.

Comparisons with the Monte Carlo model of Meier and Lee [1982], modified for the $O^+$ 834 Å problem, have shown good agreement for total volume excitation rates over the entire range of Chapman parameter space covered by the tests. The PEGFAC code of Strickland and Meier [1982], with updated cross sections [Meier, 1991; Link, private communication, 1994], provides the initial source term, $j_0$ , in Equation (A1). We are presently developing a synthesis of the initial source term (i.e., the g-factor) based on recent theoretical work by Meier [Majeed et al., 1993].

# References

Abramowitz, M., and I. A. Stegun, *Handbook of Mathematical Functions with Formulas, Graphs, and Mathematical Tables*, Dover, New York, 1972.

Anderson, D. E., and R. R. Meier, The OII 834 Å dayglow: a general model for excitation rate and intensity calculations, *Planet. Space Sci., 33,* 1179, 1985.

Anderson, D. N., M. Mendillo, and B. Herniter, A semi-empirical low-latitude ionospheric model, *Radio Science, 22,* 292, 1987.

Chamberlain, J. W., and D. M. Hunten, *Theory of Planetary Atmospheres*, Academic Press, San Diego, 1987.

Christensen, A. B., D. C. Kayser, J. B. Pranke, P. R. Straus, D. J. Gutierrez, S. Chakrabarti, R. P. McCoy, R. R. Meier, K. D. Wolfram, and J. M. Picone, Instrumentation on the Remote Atmospheric and Ionospheric Detection System experiment: extreme ultraviolet spectrometer, photometer, and near-infrared spectrometer, *Optical Engineering, 32,* 3054, 1993.

Dymond, K. F., R. P. McCoy, S. E. Thonnard, S. A. Budzien, D. D. Cleary, and T. N. Bullett, F region electron densities derived from an analysis of the $O^+$ 834 Å emission observed from sounding rockets, *J. Geophys. Res*, in preparation, 1995.

Eriksson, K. B. S., Accurate wavelengths in OII, *J. Opt. Soc. Am., 4,* 1369, 1987.

Hedin, A. E., MSIS-86 thermospheric model, *J. Geophys. Res., 92,* 4649, 1987.

Ho, Y. K., and R. J. W. Henry, Oscillator strengths and collision strengths for O II and O III, *Astrophys. J., 264,* 733, 1983.

Holstein, T., Imprisonment of resonance radiation in gases, *Phys. Rev., 72,* 1212, 1947.

Kelley, M. C. and R. A. Heelis, *The Earth's Ionosphere, Plasma Physics and Electrodynamics*, Academic Press, San Diego, 1989.

Kelley, O. A., J. M. Picone, K. F. Dymond, R. R. Meier, R. P. McCoy, and R. J. Thomas, Retrieval of the ionospheric $O^+$ concentration from 834 Å airglow using discrete inverse theory I. The Chapman layer representation, paper B19, *CEDAR '94*, Boulder, CO, 1994.

Krylov, V. I. (translated by A. H. Stroud), *Approximate Calculation of Integrals*, Macmillan, New York, 1959.

Link, R., J. S. Evans, and G. R. Gladstone, The $O^+$ 834 Å dayglow: revised cross sections, *J. Geophys. Res., 99*, 2121, 1994.

Majeed, T., D. J. Strickland, J. A. Roberts, R. Link, R. R. Meier, and J. M. Picone, An accurate, fast parameterization of dayglow volume emission rates, *EOS, Trans. Am. Geophys. Union, 74, 1993 Fall Meeting Supplement*, 465, 1993.

McCoy, R. P., D. E. Anderson, Jr., and S. Chakrabarti, $F_2$ region ion densities from analysis of $O^+$ 834-Å airglow: a parametric study and comparisons with satellite data, *J. Geophys. Res., 90*, 12257, 1985.

McCoy, R. P., R. R. Meier, K. D. Wolfram, J. M. Picone, S. E. Thonnard, G. G. Fritz, J. S. Morrill, D. A. Hardin, A. B. Christensen, D. C. Kayser, J. B. Pranke, and P. R. Straus, Far-ultraviolet imaging spectrograph and scanning grating spectrometers for the Remote Atmospheric and Ionospheric Detection System, *Optical Engineering, 33*, 430, 1994a.

McCoy, R. P, K. F. Dymond, G. G. Fritz, S. E. Thonnard, R. R. Meier, and P. A. Regeon, Special Sensor Ultraviolet Limb Imager: an ionospheric and neutral density profiler for the Defense Meteorological Satellite Program satellites, *Optical Engineering, 33*, 423, 1994b.

McCoy, R. P., Optical remote sensing of the mesosphere, thermosphere and ionosphere, in *Platforms and Systems, W. L. Barnes and B. J. Horais, Editors, Proc. SPIE 2317*, 102, 1995.

Meier, R. R. and J.-S. Lee, An analysis of the O I 1304 Å dayglow using a Monte Carlo resonant scattering model with partial frequency redistribution, *Planetary Space Sci., 30*, 439, 1982.

Meier, R. R., Ultraviolet spectroscopy and remote sensing of the upper atmosphere, *Space Sci. Rev., 58*, 1, 1991.

Meier, R. R., and J. M. Picone, Retrieval of absolute thermospheric concentrations from the far UV Dayglow: an application of discrete inverse theory, *J. Geophys. Res., 99, 6307*, 1994.

Menke, W., *Geophysical Data Analysis: Discrete Inverse Theory, Intl. Geophys. Ser., No. 45*, Academic, San Diego, 1989.

Ortland, D. A., P. B. Hays, W. R. Skinner, A. R. Marshall, M. B. Burridge, D. A. Gell, J.-H. Yee, and V. J. Abreu, The sequential estimation technique used to retrieve wind profiles from measurements made by HRDI on UARS, in preparation, 1993.

Picone, J. M., K. F. Dymond, R. R. Meier, R. P. McCoy, O. Kelley, and R. J. Thomas, Retrieval of the ionospheric $O^+$ concentration from O II 834 Å airglow using discrete inverse theory II. Diagnostics and enhancements, *EOS, Trans. Am. Geophys. Union/Supplement (Paper SA32A-21, AGU Spring Meeting)*, 83, June 21,1994.

Picone, J. M., O. Kelley, R. J. Thomas, R. R. Meier, K. F. Dymond, and R. P. McCoy, Retrieval of the ionospheric $O^+$ concentration from O II 834 Å airglow using discrete inverse theory II. Nonideal cases, *J. Geophys. Res.*, in preparation, 1995a.

Picone, J. M., O. Kelley, R. J. Thomas, R. R. Meier, K. F. Dymond, and R. P. McCoy, Retrieval of the ionospheric $O^+$ concentration from O II 834 Å airglow: different Chapman layers with "nearly identical" intensity profiles, *Geophys. Res. Lett.*, in preparation, 1995b.

Press, W. H., B. P. Flannery, S. A. Teukolsky, and W. T. Vetterling, *Numerical Recipes: The Art of Scientific Computing*, Cambridge University Press, New York, 1989.

Rodgers, C. D., Retrieval of atmospheric temperature and composition from remote measurements of thermal radiation, *Rev. Geophys. and Space Phys., 14*, 609, 1976.

Strickland, D. J. and T. M. Donahue, Excitation and radiative transport of OI 1304 Å resonance radiation – I. The dayglow, *Planet. Space Sci., 18*, 661, 1970.

Strickland, D. J. and M. H. Rees, The OI $\lambda$1304 and $\lambda$1356 emissions in aurorae, *Planet. Space Sci., 22*, 465, 1974.

Strickland, D. J., and R. R. Meier, A photoelectron model for the rapid computation of atmospheric excitation rates, NRL Memorandum Report 5004, Naval Research Laboratory, 1982.

Tarantola, A., and B. Valette, Generalized nonlinear inverse problems solved using the least squares criterion, *Rev. Geophys. Space Phys., 20*, 219, 1982.

Tarantola, A., *Inverse Problem Theory: Methods for Data Fitting and Model Parameter Estimation*, chapter 4, Elsevier, New York, 1987.

# Figures

1.   Results of DIT retrieval for a Chapman layer with true $[N_{max}, H] = [1.0 \times 10^6 \text{ cm}^{-3}, 60$ km] and $z_{max} =$ (a), (b) 250 km and (c), (d) 350 km. Panels (a) and (c) show respective profiles of the DIT retrieved $O^+$ number density versus altitude (solid line) and error bars derived from Equation (9). The retrieved parameters and $1\sigma$ uncertainties are $[0.94 \times 10^6$ cm$^{-3}$, 255 km, 61 km] and [33%, 2.9%, 1.9%] for $z_{max} = 250$ km and $[0.98 \times 10^6$ cm$^{-3}$, 356 km, 60 km] and [4.1%, 2.4%, 1.8%) for $z_{max} = 350$ km. Panels (b) and (d) show respective synthetic intensity data (short vertical lines with horizontal $\pm \sqrt{N}$ error bars) and the DIT intensity fit (solid line).

2.   Retrieved $O^+$ number density profiles and corresponding intensity profiles for cases 1 and 4 of Table 2 with true parameters given by the baseline case $[N_{max}, z_{max}, H] = [1.0 \times 10^6$ cm$^{-3}$, 350 km, 60 km]. Diagrams (a) and (b) depict typical results when starting the iterative DIT process with Chapman parameters that are "high" $[1.0 \times 10^7$ cm$^{-3}$, 600 km, 120 km]. Diagrams (c) and (d) correspond to "low" initial estimates $[5.0 \times 10^5$ cm$^{-3}$, 250 km, 30 km]. The dashed lines show the initial DIT ion concentration and intensity profiles; the solid lines show the final DIT results; the dotted lines show the true ion density profiles; and the plus (+) signs show the synthetic data, generated with different random noise for the two cases.

3.   Contour plots of the $1\sigma$ uncertainties in the retrieved $[N_{max}, z_{max}, H]$, with each $1\sigma$ value being expressed as a percentage of the respective true parameter value. The first three plots show $\sigma(N_{max})$ as a function of the true values of (a) $N_{max}$ and $z_{max}$ when the true scale height $H = 60$ km, (b) $N_{max}$ and $H$ when the true $z_{max} = 250$ km and (c) $z_{max}$ and $H$ when the true $N_{max} = 1.0 \times 10^6$ cm$^{-3}$. Plots (d), (e), and (f) show $\sigma(z_{max})$ and correspond to (a), (b), and (c), respectively. Similarly plots (g), (h), and (i) show $\sigma(H)$.

4.   Typical plots of the standard deviation of the retrieved number density values for the concentration scalar model as compared to the three-parameter Chapman layer model, when true values are given by (a) baseline case, $[N_{max}, z_{max}, H] = [1.0 \times 10^6$ cm$^{-3}$, 350 km, 60 km], and (b) - (f) baseline values with the exception of the parameter indicated. The + signs indicate CSM results for the respective cases. Dotted lines indicate the uncertainties resulting from a three-parameter Chapman layer representation.
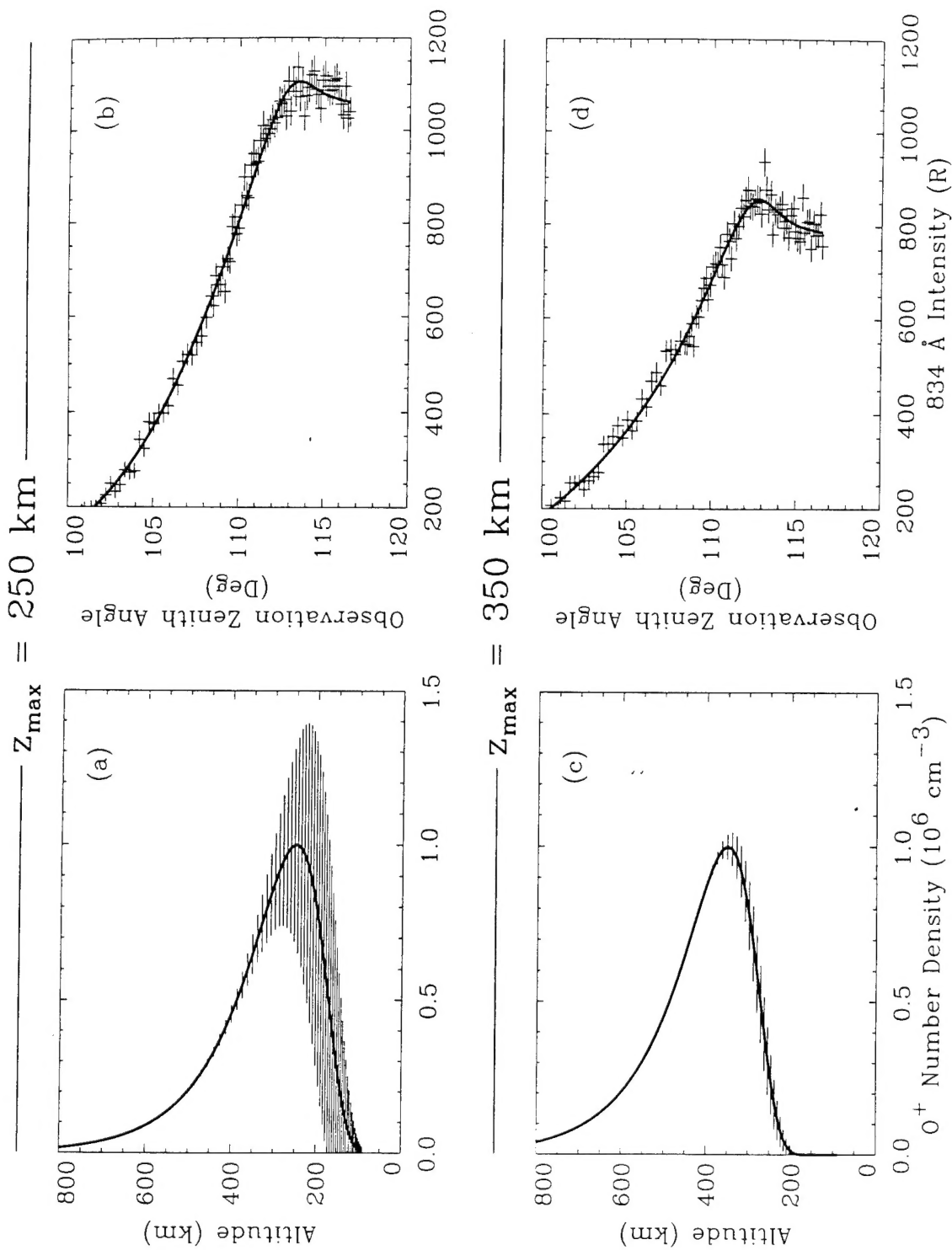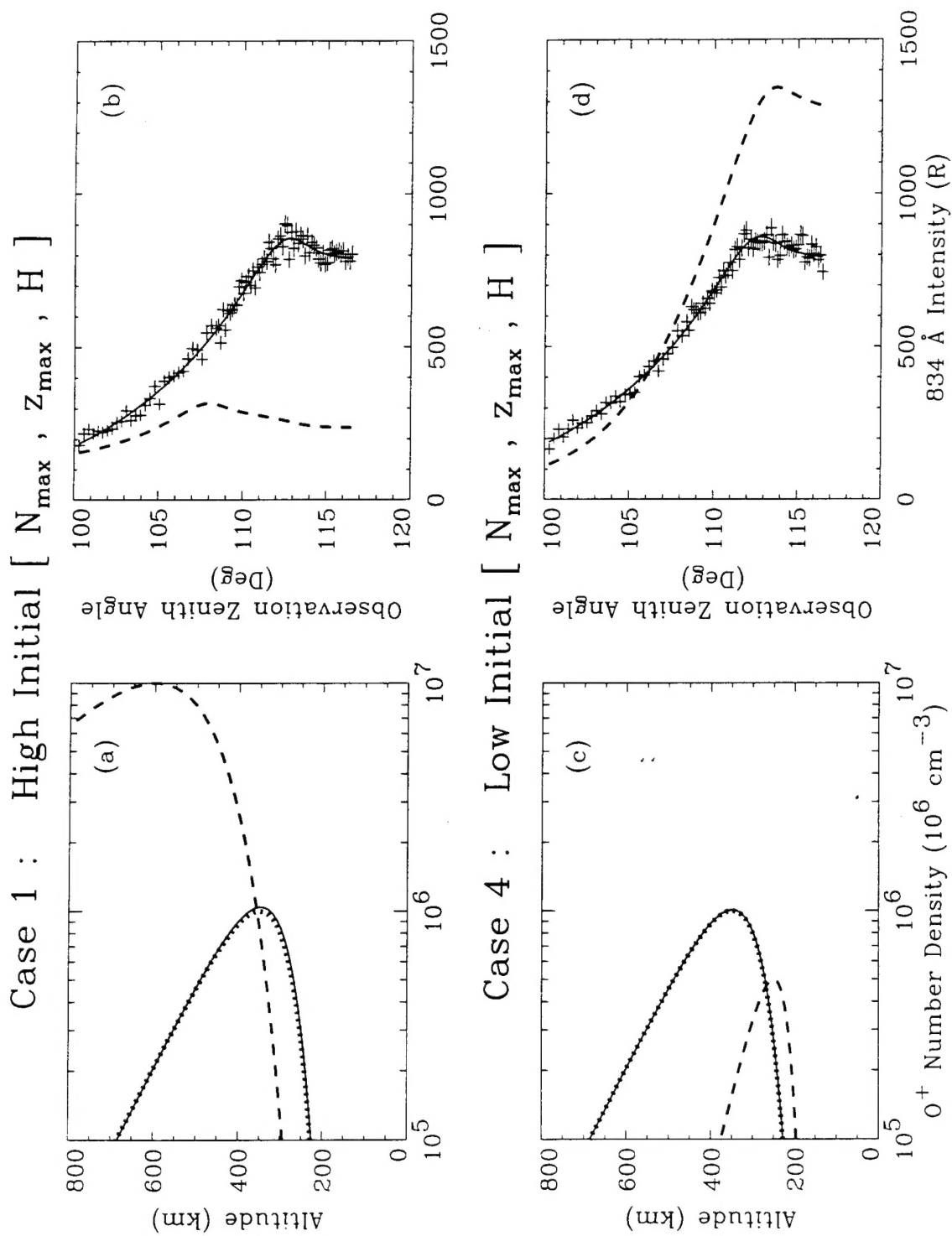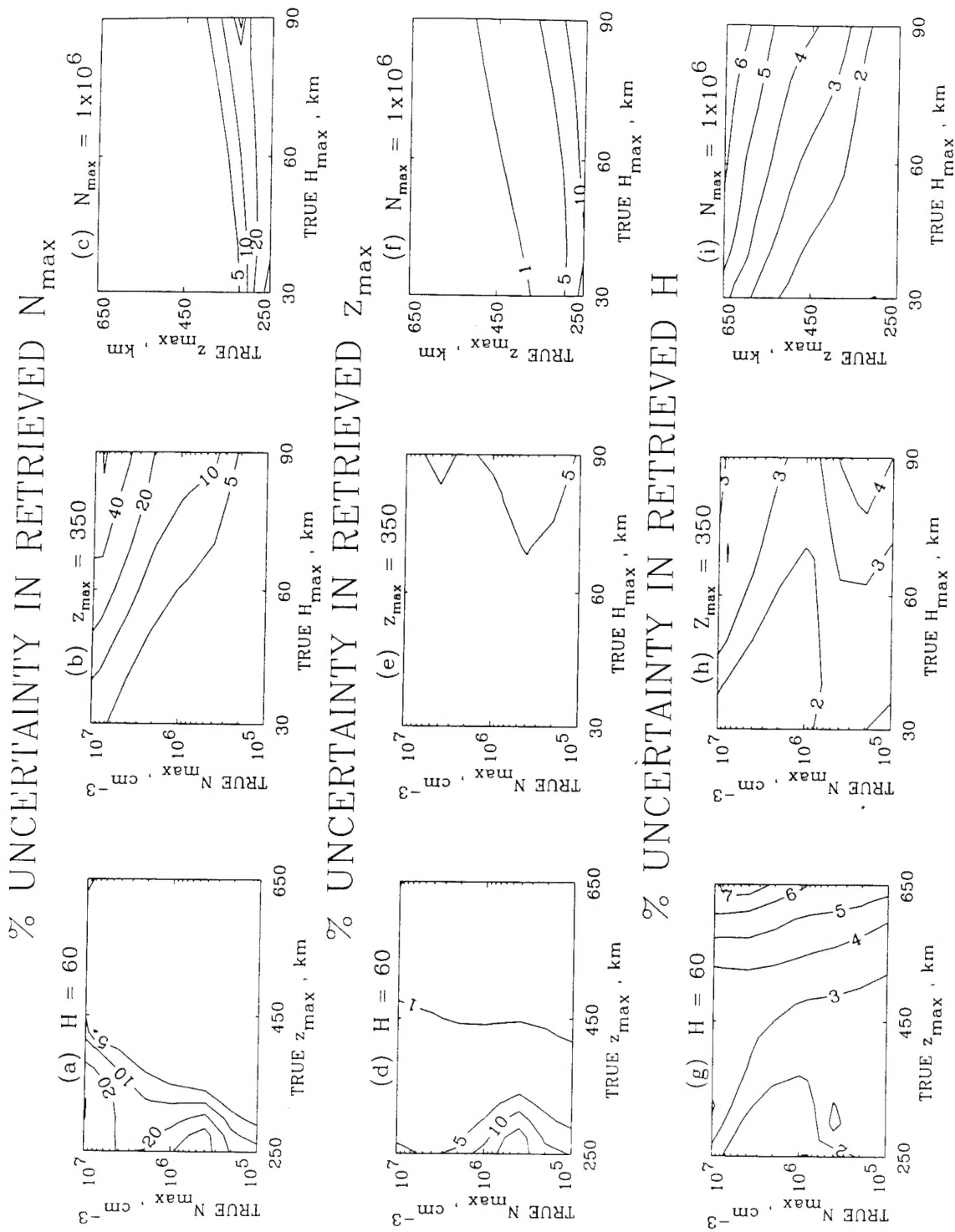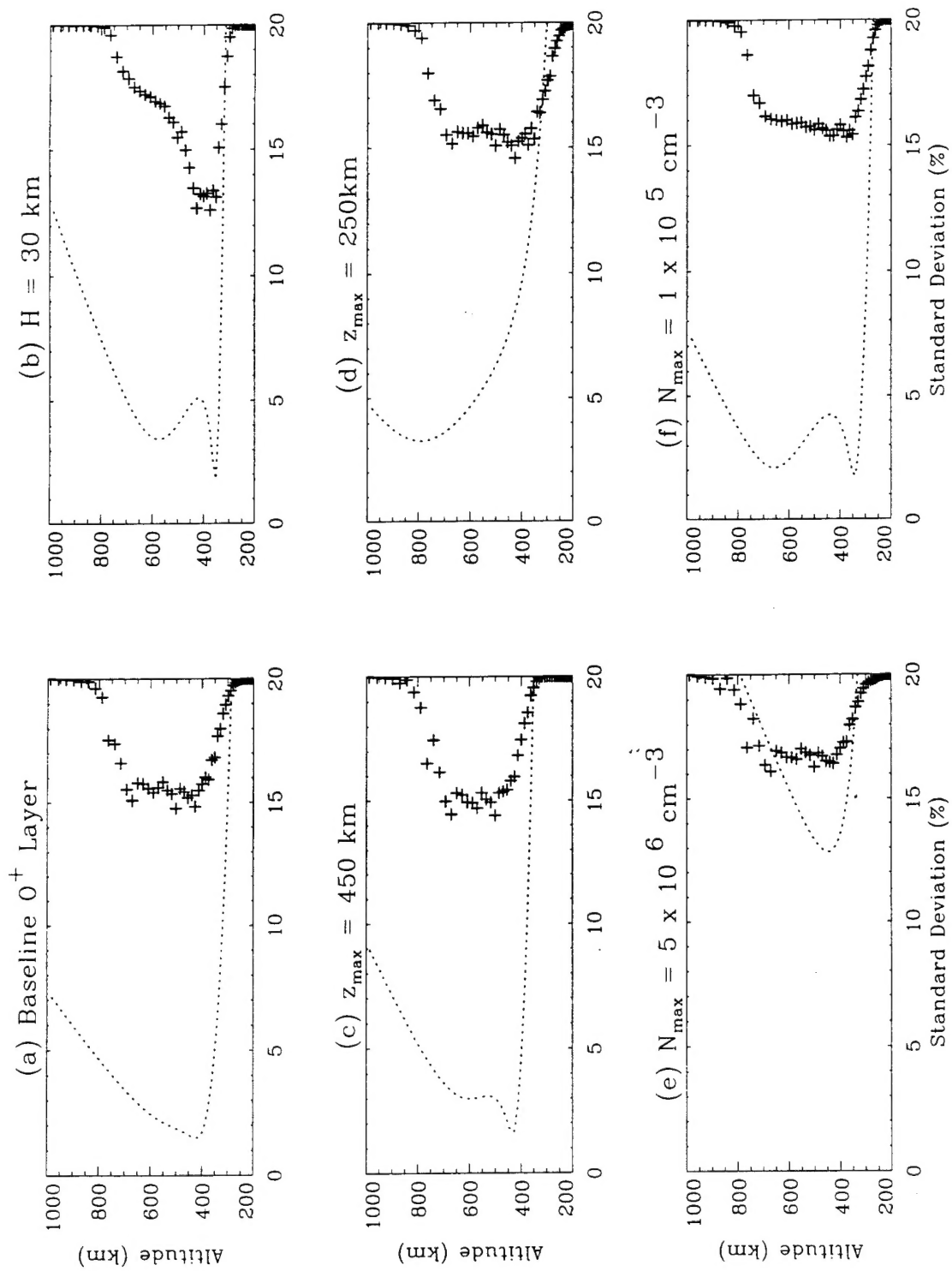
Figure 1

32

Case 1 : High Initial [ $N_{max}$ , $z_{max}$ , H ]

Case 4 : Low Initial [ $N_{max}$ , $z_{max}$ , H ]

Figure 2

Figure 3

(a) Baseline O$^+$ Layer

(b) H = 30 km

(c) $z_{max}$ = 450 km

(d) $z_{max}$ = 250km

(e) $N_{max}$ = 5 x 10$^6$ cm$^{-3}$

(f) $N_{max}$ = 1 x 10$^5$ cm$^{-3}$

Figure 4

Altitude (km)

Standard Deviation (%)

35